

# Three-Antenna Doppler-Delay Imaging of the Crater Tycho for Uplink Array Calibration Applications

V. Vilnrotter,<sup>1</sup> D. Lee,<sup>1</sup> R. Mukai,<sup>1</sup> T. Cornish,<sup>1</sup> and P. Tsao<sup>1</sup>

*Uplink arrays have the potential to greatly increase NASA's deep-space command and communications capabilities and to provide greater reach during spacecraft emergencies. However, due to long round-trip light times, it is not practical to phase up and track the carrier phase of each antenna element using real-time measurements at the spacecraft. This article describes a method for utilizing the Moon as a natural far-field reflector for calibrating uplink arrays by extending well-known Doppler-delay radar imaging techniques to an array of transmitting antennas. A small, highly reflective feature on the Moon is selected as the calibration target, and the phase vector corresponding to maximum reflected power from the target is selected. The theoretical basis of "Moon-bounce" calibration is presented, and experimental results obtained with arrays of up to three 34-m antennas of the Deep Space Network are described.*

## I. Introduction

This article describes a potential technique for calibrating uplink arrays using Doppler-delay imaging of localized high-reflectivity targets on the Moon. Doppler-delay imaging of the Moon using a single transmitting antenna has been described in [1]. The extension of the single-antenna technique to an array of antennas, specifically to the simplest array consisting of two antennas, has been proposed and described in [2], with the main ideas summarized in Section III.

The Moon is in the far field of uplink arrays considered for future use. Far-field calibration techniques are advantageous because they require only direction ephemerides, not range, thereby eliminating one of the more problematic parameters from the calibration process. Far-field calibration also provides the opportunity to measure the combined power beamed in a given direction, such as towards the calibration target, thus providing simultaneous verification of successful calibration through the process of power maximization. Although receive-mode uplink array calibration using well-known interferometric synthetic-aperture radar (SAR) techniques is theoretically feasible, as described in [2], the preferred method for calibrating an uplink array is in transmit mode, in which all of the array elements transmit

---

<sup>1</sup> Communications Architectures and Research Section.

The research described in this publication was carried out by the Jet Propulsion Laboratory, California Institute of Technology, under a contract with the National Aeronautics and Space Administration.

simultaneously towards a predetermined direction in space, and the far-field signal power is maximized in this direction through direct power measurements.

## II. Link budget for Moon-Bounce Calibration

Highly reflective features on the Moon, such as the center of the crater Tycho, provide a convenient target for uplink array calibration using this technique, termed “Moon-bounce calibration” in the rest of this section. The lunar surface imparts different Doppler shifts to radio signals reflected from thin “slices” parallel to the apparent spin axis of the Moon. In addition, the near-spherical mean surface of the Moon can be decomposed into concentric rings of equal distance, or delay, from the receivers, with radii increasing from the apparent center of the Moon [1]. The intersection of the Doppler slices and concentric delay rings gives rise to “pixels” on the lunar surface with distinct Doppler-delay signatures, which can be used to isolate specific features on the lunar surface.

The signal power reflected from a kilometer-sized target on the Moon and the resulting signal-to-noise ratio (SNR) can be estimated using a simplified link budget that assigns beamwidths to the array antennas as well as to the entire array, and that assumes a simple scattering surface with a given bulk reflectivity at the Moon. Although nominally presenting the same face towards the Earth at all times, the Moon actually exhibits a small apparent spin called libration, the largest component of which is the time-varying parallax due to Earth rotation, called diurnal libration. The other components are called longitude and latitude libration. The maximum apparent spin rate of the Moon due to diurnal libration for an observer at the Earth’s equator is approximately  $1.2 \times 10^{-6}$  rad/s at transit [3]. This implies that approaching and receding limbs at the lunar equator appear to move toward or away from the Earth at a velocity of approximately  $v = \pm R_{\text{Moon}}\omega = (1.75 \times 10^6)(1.2 \times 10^{-6}) \cong 2$  m/s. At a carrier frequency of 7.15 GHz, this apparent lunar rotation rate produces Doppler frequencies of approximately  $f_D = \pm f(v/c) = \pm(7.15 \times 10^9)(2/3)10^{-8} \cong \pm 50$  Hz. Longitude libration has a maximum value of  $4 \times 10^{-7}$  rad/s, which could add or subtract directly to the diurnal libration at certain times of the month [3]. The maximum value of latitude libration is slightly less, approximately  $3.5 \times 10^{-7}$  rad/s; however, this spin vector is perpendicular to the other two, causing a tilt in the apparent spin axis. When all three components are simultaneously at their maximum value, the resulting spin is approximately  $1.64 \times 10^{-6}$  rad/s, yielding maximal Doppler frequencies of  $\pm 70$  Hz at the limbs, or a limb-to-limb Doppler spread of 140 Hz. However, most of the time the actual Doppler spread is less: a reasonable average value for use in link-budget calculations is the maximal diurnal rate of  $\pm 50$  Hz, resulting in a limb-to-limb Doppler spread of 100 Hz.

Geometrical arguments reveal that at any time the Doppler spread is distributed uniformly over the Moon, yielding slices of constant Doppler frequency parallel to the spin axis. Since the diameter of the Moon is approximately 3500 km, the change in Doppler frequency over 1 km perpendicular to the spin axis is  $100/3500 \cong 0.03$  Hz/km. Since the Moon is essentially spherical, signals reflected from the point nearest the Earth are delayed less at the receiver than those reflected from the limbs. Because signals reflected by features some distance from the apparent lunar center travel the extra distance twice, the total delay spread of the Moon can be expressed as  $\delta = 2R_{\text{Moon}}/c = 3.5 \times 10^6/3 \times 10^8 \cong 12$  ms. If the lunar surface is inclined at 45 deg to the signal propagation vector, as near the crater Tycho, then a 1-km target on the Moon requires range resolution of approximately  $1/1.414 = 0.707$  km. It follows that calibration techniques utilizing kilometer-sized pixels on the Moon as radar reflectors should be designed with a frequency resolution of 0.03 Hz and a range resolution of roughly 700 m. Such a frequency resolution can be obtained easily by means of efficient fast Fourier transforms (FFTs), while the required range resolution can be obtained using maximal-length pseudonoise (PN) sequences, as described in more detail in Section V, Experimental Results, of this article.

As an example of the achievable SNR and other relevant parameters required for Moon-bounce calibration, consider the use of kilometer-sized pixels with a power-reflection coefficient of approximately 0.01

at 7.15 GHz. Power reflectivity could actually be as large as 0.03 near the crater Tycho [4], so the value used in this calculation is somewhat conservative. An array of two  $d = 34$  m beam-waveguide (BWG) antennas separated by  $D = 340$  m yields a maximal primary beamwidth of approximately  $\lambda/d = 0.04/34 = 1.2$  mrad where  $\lambda$  is wavelength, equal to 4 cm at 7.15 GHz, and a minimal array beamwidth of  $\lambda/D = 0.12$  mrad, forming a fan-shaped beam with array peaks and nulls perpendicular to the baseline. At the distance of the Moon, a 1-km pixel inclined at 45 deg to the propagation vector subtends maximal and minimal divergence angles of  $1/400,000 = 2.5 \mu\text{rad}$  and  $2.5/1.414 = 1.77 \mu\text{rad}$ , respectively. If each antenna transmits 20 kW, the power density in space due to a single antenna is approximately  $20,000/10^{-6} \cong 2 \times 10^{10}$  W/sr, but actually a factor of 4 greater over peaks of constructive interference. A 1-km pixel at an inclination of 45 deg subtends  $4.4 \times 10^{-12}$  sr; hence, it collects  $(8 \times 10^{10})(4.425 \times 10^{-12}) = 0.35$  W. Since the lunar surface is rough, it behaves somewhat like a Lambertian scatterer, but it often scatters radio signals into a more concentrated cone than the cosine law would indicate. For this link-budget calculation, we shall assume that most of the scattered signal power is contained in an octant covering  $\pi/2$  sr. Since a 34-m receiving antenna at the distance of the Earth subtends  $6 \times 10^{-15}$  sr from the Moon, the power collected from a 1-km pixel by the receiving antenna, with a bulk reflectivity in the direction of the receiver of 0.01, is on the order of  $0.02 \times 0.354 \times (6 \times 10^{-15})/\pi = 1.4 \times 10^{-17}$  W. Since the Doppler spread over 1 km is only 0.03 Hz, the entire signal power from the target pixel is contained within this bandwidth. The spectral level of thermal noise for an ideal room-temperature receiver is  $\kappa T = 300(1.38 \times 10^{-23}) \cong 4 \times 10^{-21}$  W/Hz; hence, the ratio of signal power to noise power in a bandwidth of 0.03 Hz is  $(1.4 \times 10^{-17})/(0.03 \times 4 \times 10^{-21}) = 1.2 \times 10^5$ , or about 51 dB. Achieving 0.03-Hz bandwidths requires integration time of at least 30 s in duration; however, that is a reasonable measurement time for this application. It is clear that thermal noise will not be the limiting factor in determining uplink array calibration performance. The limiting factor with matched filters observing the sum of a large number of delayed maximal-length PN sequences, each weighted by the appropriate reflection coefficient, tends to be self-interference due to the fact that delayed versions of maximal-length PN sequences are not exactly orthogonal.

### III. Mathematical Model of the Signal Processing Algorithm

The geometrical relationship between two transmitting antennas and a single receiving antenna designed to collect reflected signal power from Doppler-delay pixels is shown in Fig. 1. Radar imaging applications suggest that a PN sequence modulated carrier should be used in order to achieve the desired range resolution. For transmit-mode calibration, it is necessary to take into account the time-varying range to the target at each transmitting antenna. If the array antennas were stationary in the reference frame of the lunar target, the transmitted signals at the  $i$ th antenna could be represented in complex form as  $x_i(t) = \sqrt{P_t}m(t) \exp[j(\omega t + \theta_i)]$ , where  $m(t)$  is an appropriate PN modulation,  $\omega = 2\pi f$  is the common carrier radian frequency,  $P_t$  is the transmitted power, and  $\theta_i$  is a slowly varying phase term describing equipment drift and possible thermal expansion in the signal distribution network of the  $i$ th antenna. However, due to relative motion between the antennas and the lunar target, the distance between the lunar target and the  $i$ th antenna changes continuously. Without compensating for the time-varying delay, the transmitted signal from the  $i$ th antenna,  $1 < i < N$ , in the reference frame of the lunar target, can be expressed as  $x_i(t) = \sqrt{P_t}m(t - [R_i(t)/c]) \exp[j(\omega t + [2\pi R_i(t)/\lambda_1] + \theta_i)]$ , where  $R_i(t)$  is the time-varying differential distance to a specific lunar feature.

One way to accomplish phase compensation is by introducing time-varying delays into the signal paths by means of mechanical line stretchers; however, this approach is neither cost effective nor practical. A more useful approach can be perceived by expressing the time-varying ranges in a Taylor's series expansion around the center of the observation interval, arbitrarily denoted as  $t = 0$ . Let  $R_i(0) = R_i$ , and expand the  $i$ th time-varying differential range in a neighborhood around  $t = 0$  as

$$R_i(t) = R_i + t \frac{\partial R_i(t)}{\partial t} + \sum_{i=2}^{\infty} \frac{t^i}{i!} \frac{\partial^i R_i(t)}{\partial t^i} \quad (1)$$

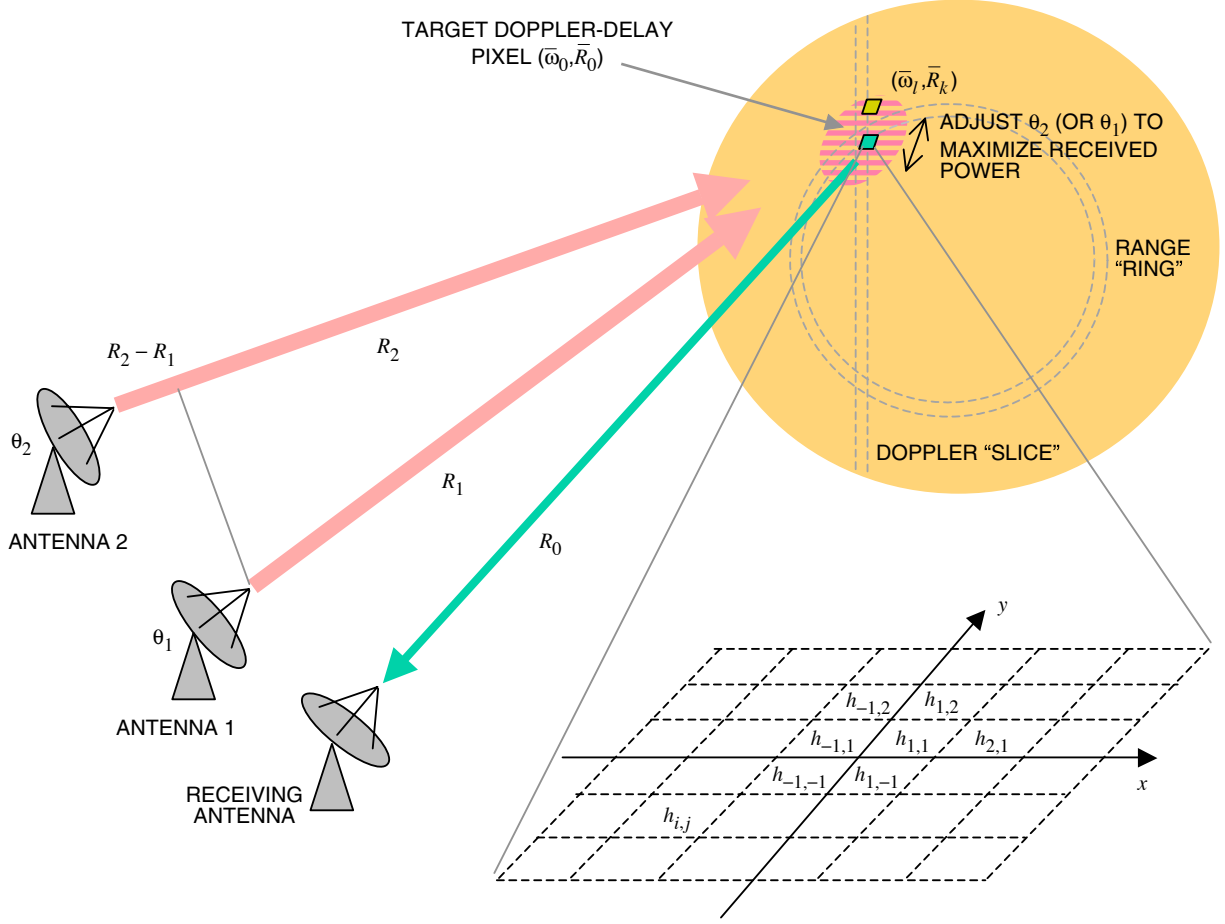


**Fig. 1. Transmit mode uplink array calibration concept, illustrating electronic scanning of the far-field signal distribution by varying the differential antenna phase. The insert shows partitioning of the target pixel into independent sub-pixels, representing individual scatterers.**

where the derivatives are evaluated at  $t = 0$ . For the case when the differential range varies slowly over the measurement interval, such as uplink array calibration by means of Moon-bounce, the first two terms in Eq. (1) provide an accurate description of the differential range. Denoting  $\Delta\omega_i = 2\pi(f/c)\partial R_i(t)/\partial t$ , and further defining  $\omega_i = \omega + \Delta\omega_i$ , the transmitted signal from the  $i$ th antenna can be expressed as the sum of the quiescent carrier frequency, plus a Doppler frequency due to the  $i$ th velocity component, plus a static phase term that accounts for initial propagation delays:  $x_i(t) = \sqrt{P_t}m(t - [R_i/c]) \exp[j(\omega_i t + [2\pi R_i/\lambda] + \theta_i)]$ ,  $1 < i < N$ . Therefore, a viable option for compensating time-varying delays between antennas is to pre-compute the Doppler frequencies associated with each antenna and apply them to the signal prior to transmission, thus ensuring that the carrier frequencies arriving from each antenna will be identical at the lunar target, equal to the quiescent frequency in the static model. Note that it is necessary to compensate differences only in delay and phase among the various antennas, for example, the phase and delay differences between two antennas, as shown in Fig. 1. Differential delays and differential initial phases can be pre-computed and applied, leaving only the residual phase due to equipment instabilities and signal distribution effects undetermined. Using the uplink array in this mode is referred to as Doppler-delay compensated operation.

Assuming ideal Doppler-delay compensation by means of pre-computed geometry-based predicts, the sum of the fields impinging on a point at the lunar surface from two antennas is of the form  $y(t) = C'[\exp(j\theta_1) + \exp(j\theta_2)]m(t)\exp(j\omega t) \equiv C'm(t)\exp(j\omega t)$ , where  $C'$  is a complex constant that accounts

for propagation losses and delays and  $\omega$  is the quiescent carrier frequency, common to each compensated carrier at the lunar surface.

Consider a point on the lunar surface where the different Doppler frequencies and range differences have been properly compensated. For reasonable array geometries, it can be shown that Doppler frequencies are also effectively compensated over a region of several hundred kilometers at the distance of the Moon. Under these conditions, it is clear that if  $\theta_1 = \theta_2$  at a given point on the surface, the impinging fields are in phase. The magnitude of the illuminating field at this point on the lunar surface is twice that of a single antenna; hence, the combined signal power is a factor of four greater than that from either antenna individually. Similarly, if the phase of the second (or first) antenna differs from that of the first (or second) antenna by  $\pi$  rad, the power over this point is reduced to zero. For compensated points on the lunar surface within the overlapping footprint of the two antennas, the fields cancel or reinforce depending on the residual electronic phases on the ground.

If the residual electronic phases are equal at the compensated point,  $\theta_1 = \theta_2$ , then the magnitude of the complex constant  $C$  is proportional to twice the field magnitude contributed from each antenna. This can be incorporated into the model by expressing the magnitude of the complex coefficient at a point  $\xi$  as  $|C| \propto 2\sqrt{P_t}$ ,  $\theta_1 = \theta_2$ . When the residual electronic phases denoted by  $\theta_1$  and  $\theta_2$  are not equal, then the magnitude of the complex coefficient takes the form  $|C| \propto \sqrt{P_t} |\exp(j\theta_1) + \exp(j\theta_2)| = \sqrt{2P_t [1 + \cos(\theta_2 - \theta_1)]} \equiv \sqrt{2P_t (\Delta\theta)}$ , showing that the power is a function of the electronic phase difference  $\Delta\theta \equiv \theta_2 - \theta_1$ . Once the residual phases have been compensated over a point on the lunar surface for two antennas, it follows from geometrical considerations that the phases remain essentially compensated along a line or thin strip perpendicular to the plane defined by the two-antenna baseline and passing through the compensated point, to the extent of the beam, at any instant of time. However, along a line parallel to the baseline, additional differential phase is accumulated as we move away from the compensated point, leading to periodic cancellation and reinforcement of the combined fields.

This results in bands of constructive and destructive interference in the far field of the two-antenna array, which can be clearly discerned in Doppler-delay images of the lunar surface coherently illuminated with two antennas. Similar arguments hold for three or more antennas, with the pattern of constructive and destructive interference becoming increasingly more complex. Examples of actual two- and three-antenna patterns reflected from the lunar surface will be provided in the following section.

At the lunar surface, the radio wave impinging on the lunar target can be represented as a plane wave. After encountering the rough lunar surface, a fraction of the signal field is reflected, with a still smaller fraction propagating directly toward the transmitter. Since scatterers on the surface are at slightly different distances from the transmitter, the phase of each reflected component is a random process with a time constant on the order of milliseconds. Consider the Cartesian coordinate system attached to the lunar surface, as shown in the inset in Fig. 1. The reflected fields can be modeled as the product of a reflected plane wave and an amplitude and phase distortion function,  $h(x, y)$ . A specific region of the lunar surface with a well-defined Doppler-delay signature that can be isolated by means of matched-filter processing is called a resolution pixel, or pixel for short. Within a pixel, there is a multitude of scatterers, each behaving as a point source imparting a different phase to the reflected signal component. With this interpretation, we can effectively replace the continuous lunar surface within a given pixel with a grid of complex samples. This sampled model is illustrated in Fig. 1, where several scattering coefficients, as well as the general sample, are indexed by  $(i, j)$  to demonstrate the notational convention used in the subsequent analysis. However, for the purpose of accounting for the contribution of scatterers within a pixel, the double notation is not necessary, and a single subscript  $n$  can be used instead to enumerate the scatterers.

After encountering the lunar surface, a Doppler frequency generated by an effective lunar spin is added to the carrier frequency of the reflected components. Each reflecting surface within the selected pixel has approximately the same relative radial velocity, and approximately the same range, as any other.

Adjacent pixels, on the other hand, have slightly different rotational velocities, or range, or both from the selected pixel. Denoting the average Doppler-shifted carrier frequency and average range from the selected pixel by  $(\bar{\omega}_0, \bar{R}_0)$ , respectively, and those from the  $kl$ th pixel by  $(\bar{\omega}_k, \bar{R}_l)$ , and assigning a random complex reflection coefficient  $h_{kl}(n)$  to the  $n$ th reflecting surface within the  $kl$ th pixel, the received signal from the  $kl$ th pixel contains all reflected components from that pixel and hence is of the form

$$r_{kl}(t) = \sqrt{P_t} m \left( t - \frac{\bar{R}_k}{c} \right) \exp(j\bar{\omega}_l t) \sum_n h_{kl}(n) \quad (2)$$

Here propagation losses and ground antenna gains have been incorporated into the complex coefficients  $h_{kl}(n)$ . Assuming that the receiving antenna is of the same diameter as the transmitting antennas, it collects reflections from all pixels within the illuminated footprint, yielding the total received signal  $r(t) = \sum_{k,l} r_{kl}(t)$ . The reflections from the selected pixel can be isolated by correlating the received signal with a PN sequence and Doppler frequency matched to the Doppler-delay signature of the selected pixel. Denoting this function by  $m(t - [\bar{R}_0/c]) \exp(-j\bar{\omega}_0 t)$ , the result of the correlation operation is as follows:

$$\begin{aligned} & \frac{1}{T} \int_0^T r(t) m \left( t - \frac{\bar{R}_0}{c} \right) \exp(-j\bar{\omega}_0 t) dt \\ &= \frac{1}{T} \int_0^T \{r_{00}(t) + r_{01}(t) + \cdots + r_{kl}(t) + \cdots\} m \left( t - \frac{\bar{R}_0}{c} \right) \exp(-j\bar{\omega}_0 t) dt \\ &= 2\sqrt{P_t} \sum_n h_{00}(n) + (\text{delayed correlation terms close to zero}) \cong 2\sqrt{P_t} \sum_n h_{00}(n) \quad (3) \end{aligned}$$

Only those scattered components originating from the selected pixel survive the correlation operation. All other reflected components are greatly reduced by virtue of the fact that the normalized autocorrelation of the maximal-length PN sequence is close to zero for all integer shifts, and that integrals of the complex exponential function over an integer number of cycles are zero. However, the backscattered signal components interfere with the detection operation, typically contributing the dominant source of error.

Equation (3) shows that the correlation operation effectively eliminates the scattered signal field components from all but the selected pixel. Ignoring the delayed correlation terms and taking the expected value of the squared magnitude of the peak correlation yields the average reflected signal power collected by the receiver from the selected pixel:

$$4P_t E \left( \sum_n h_{00}(n) \right)^2 = 4P_t \sum_n E |h_{00}(n)|^2 + 4P_t \sum_n \sum_{\substack{m \\ n \neq m}} E h_{00}(n) h_{00}^*(m) = 4P_t \sum_n \rho_n \quad (4)$$

where  $E$  is the expectation operator and  $\rho_n = E |h_{00}(n)|^2$  is the average reflection coefficient of the  $n$ th scatterer within the selected pixel. When the interference pattern generated by the antenna pair reaches its peak over the selected pixel, the received power in the matched filter is maximized for any realization of the scattering surfaces. Higher average bulk reflectivity, characterized by larger values of  $\rho_n$  within the selected pixel, yields higher average received power; therefore, it is advantageous to search for regions of high reflectivity at the carrier frequency of interest. In practice, a large number of Doppler

frequencies are processed simultaneously by applying an FFT to each vector of samples, corresponding to every resolved delay within the delay spread of the array footprint. When the received pixel intensities are recorded on a grid representing delay and Doppler, a radar image of the illuminated region is formed. In practice the target can be identified from the radar image, and a suitable pixel or set of pixels can be selected to carry out uplink array calibration by adjusting the carrier phases at the antennas until the received power is maximized.

#### IV. Experimental Setup and Simulation

In a recent series of experiments, all three antennas at the Apollo Complex were used to illuminate the Tycho region of the Moon, first pairwise and then with all three antennas simultaneously. A picture of the three 34-m BWG antennas at the Apollo Complex, Deep Space Station (DSS) 24, DSS 25, and DSS 26, is shown in Fig. 2. The receiver used in these experiments was located at DSS 13 in the pedestal room of the 34-m BWG antenna, as shown in Fig. 3. It was necessary to develop this receiver, tuned specifically to the 7.15-GHz uplink frequency band, since the downlink frequency band of the Deep Space Network (DSN) is centered around 8.4 GHz and hence is not compatible with Moon-bounce radar imaging and uplink array calibration experiments.

Before performing the three-antenna field experiments, simulations were carried out to predict the far-field array pattern for the two- and three-antenna arrays, using the actual array geometry at the Apollo site. As described in the previous section, the far-field pattern of a two-antenna array consists of bright and dark bands resulting from constructive and destructive interference perpendicular to the baseline, shaped by the primary antenna pattern. This behavior is clearly shown in Fig. 4, for all three pairs of baselines. However, the characteristics of the intensity pattern for the three-antenna configuration cannot be deduced easily from the individual baseline intensity patterns.

The relationship between the two-antenna and three-antenna array intensity patterns can be derived by considering the interaction of the complex array fields in the far field. We will treat a simplified case of  $N$  plane waves incident on a planar surface. It will be assumed that each of the  $N$  plane waves has unit



**Fig. 2. Apollo Complex, showing the three 34-m BWG antennas DSS 26 (foreground), DSS 25, and DSS 24 (most distant).**

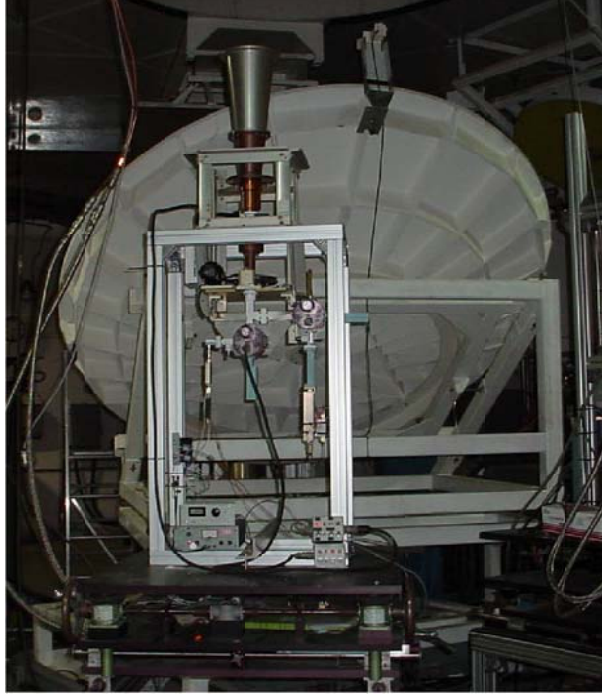


**Fig. 3. Room-temperature Moon-bounce receiver at DSS 13, tuned to a 7.15-GHz center frequency.**

amplitude. Thus, at the planar surfaces where the waves are incident, the complex field for the  $n$ th wave is given by

$$U_n(x, y) = \exp(j(k_{n,x}x + k_{n,y}y)) \quad (5)$$

where  $n$  ranges from 1 through  $N$ , and  $k_{n,x}, k_{n,y}$  are direction cosines for the  $n$ th wave. First consider the total field, which is defined as

$$U_{\text{total}}(x, y) = \sum_{n=1}^N U_n(x, y) \quad (6)$$

The maximum possible absolute value of  $U_{\text{total}}(x, y)$  is  $N$ . The condition  $|U_{\text{total}}(x, y)| = N$  is achieved when

$$\arg U_1(x, y) = \arg U_2(x, y) = \cdots = \arg U_N(x, y) \quad (7)$$

That is, the maximum absolute value of  $U_{\text{total}}(x, y)$  is always achieved at those points where all  $N$  of the signal phasors have exactly the same angle. The real amplitude of any field  $U(x, y)$  is defined as the absolute value  $|U(x, y)|$ . Intensity is defined as the squared absolute value  $|U(x, y)|^2$ . Since intensity is always a non-negative real number, the minimum possible intensity is zero.

Equation (7) is clearly also a sufficient, but not necessary, condition for the sum of any arbitrary subset of the  $N$  fields to achieve a maximum. If all  $N$  phasors are aligned, then any subset will also be



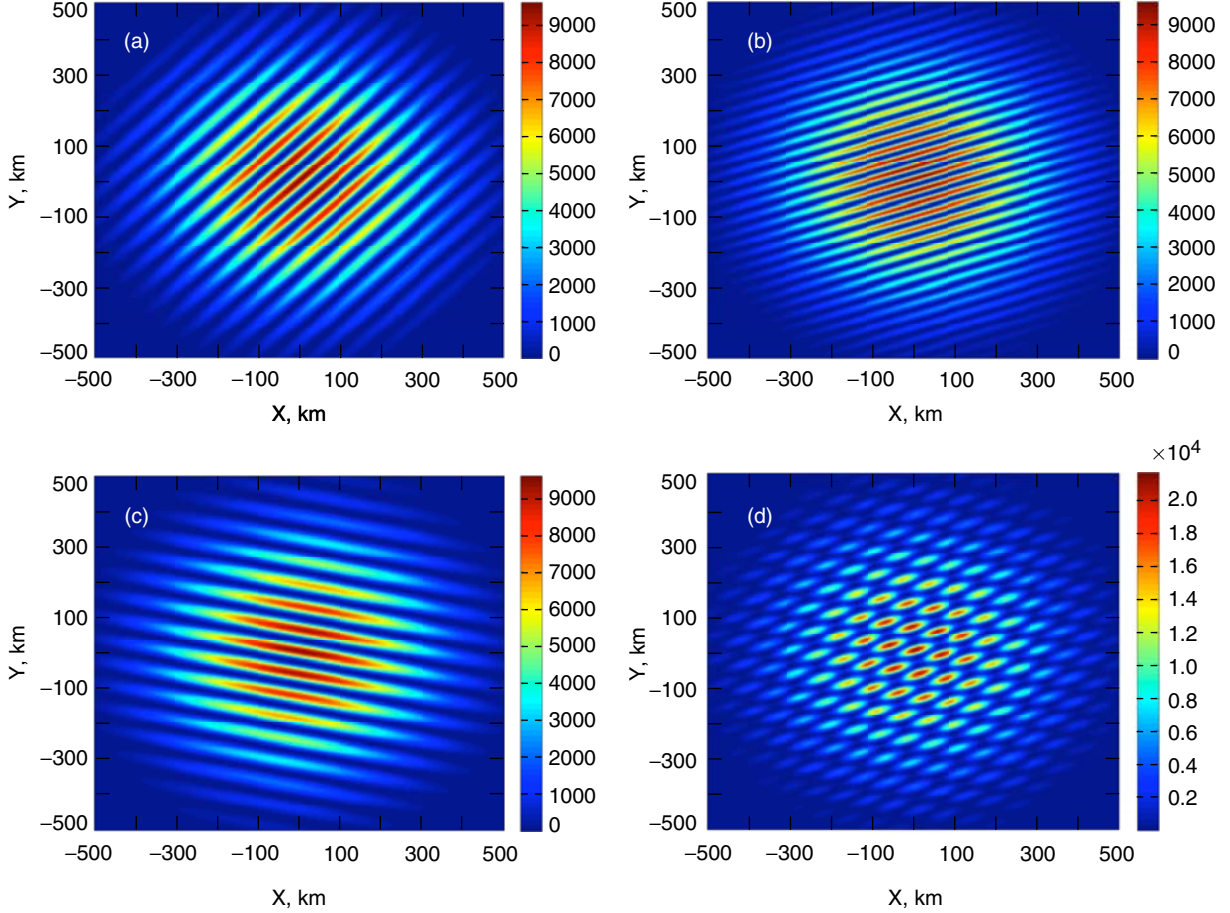


**Fig. 4. Simulated two- and three-antenna far-field intensity patterns at the distance of the Moon, corresponding to the Apollo cluster geometry: (a) DSS 25–DSS 26 baseline, (b) DSS 24–DSS 26 baseline, (c) DSS 24–DSS 25 baseline, and (d) three-antenna far-field intensity pattern. Note that the narrowest fringe space, in (b), corresponds to the longest baseline, namely, DSS 24–DSS 26.**

aligned and the sum of any subset will also achieve a maximum. However, the converse is not true. If, for example, we have  $N = 4$  and two phasors have an angle of 0 deg and two have an angle of 180 deg at a given point in the  $(x,y)$ -plane, then the amplitude of the sum of the four fields will be zero. It remains true that all maxima of the total field must correspond to a maximum of any sum of the component fields. Minima are different: a minimum of the total field may not correspond to a minimum of the sum of any subset of the component fields. Likewise, the minimum of a sum of a subset of the component fields may not correspond to a minimum of the total.

For the three-field case, if the sum of *any* two fields yields zero intensity at a point  $(x_0, y_0)$ , then since the third field has unit amplitude at  $(x_0, y_0)$  it is necessarily true that the total field also has unit amplitude at the same point  $(x_0, y_0)$ . Hence, for the case of three incoming unit amplitude plane waves with different arrival angles, any point that is a zero intensity point of the sum of any two of the three fields is always a unit intensity point of the total field. Therefore, any zero intensity point of the three-field pattern will not be a minimum intensity point of any of the three possible two-field patterns, and any zero intensity point of any of the three two-field patterns will not be a minimum intensity point of the total three-field pattern.

Furthermore, the three-field case clearly obeys the earlier rule regarding field maxima: any maximum intensity point of the total field is a maximum intensity point of any sum of any two fields of the three-

field pattern. However, it is not true that the maximum intensity points of the two-field patterns are maximum intensity points of the three-field pattern. These principles are illustrated in Fig. 4, which shows the simulated far-field intensity patterns corresponding to the three two-antenna baselines, namely, the DSS 24–DSS 25, DSS 24–DSS 26, and DSS 25–DSS 26 baselines, plus the far-field pattern of the three-antenna array, at the distance of the Moon, with zero differential phase between the baselines. It can be discerned that all maxima of the three-antenna intensity pattern also correspond to two-antenna intensity peaks; however, the converse is not necessarily true.

## V. Experimental Results

This section presents experimental results of Doppler-delay imaging of the crater Tycho and its surroundings, whose compact and highly reflective central peak provides a suitable target for uplink array calibration. The Doppler-delay calibration concept described above was implemented and tested at the Goldstone Deep Space Communications Complex (GDSCC) near Fort Irwin, California. Three identical 34-m BWG antennas at the Apollo Complex were used to form two- and three-element arrays for the field experiments. Each antenna was equipped with a 20-kW transmitter and was driven by nominally 7.15-GHz signals generated at Signal Processing Center (SPC) 10, located some 16 km away. The signals were distributed by means of fiber-optic cables using a common fiber bundle between SPC 10 and the Apollo Complex, where the cables for each antenna were separated out.

Since the antennas are several hundred meters apart, each antenna experiences a slightly different Doppler frequency due to Earth rotation as observed from a distant point in space. Therefore, slightly different Doppler frequencies must be applied to each antenna by means of pre-computed frequency predicts to ensure that each carrier arrives at the Moon with the same frequency. The reflected signal components were collected by another 34-m BWG antenna at the Venus Station, some 10 km from the Apollo Complex. Additional Doppler compensation was applied to the transmitted signals to account for the receiver location, such that the received signal arrived at the receiver centered at precisely 7.15 GHz. Frequencies were compensated for the center of the crater Tycho, which was selected as the target for these experiments.

As described above, different Doppler slices on the Moon impart different Doppler shifts to the signal, generating Doppler-broadened echoes, an example of which is shown in Fig. 5(a). The main lobe of the scattered continuous wave (CW) signal spectrum from the Tycho region is seen to be approximately 50 Hz (about 40 dB below the peak), but spectral components out to 100 Hz also can be discerned 50 to 60 dB below the peak. Since the maximum Doppler broadening generated by the lunar disk is approximately 140 Hz, these results are consistent with the expected spectral signature of an illumination pattern whose side lobes cover the entire lunar disk.

Whereas Doppler slices can be separated directly from the broadened echo even without modulating the signal, range resolution must be established by separating out delays scattered from different range rings. This operation is accomplished by modulating the carrier with a suitable PN sequence possessing good autocorrelation properties. With maximal-length PN sequences consisting of  $M = 2^L - 1$  chips (or PN symbols), peak correlation proportional to  $M$  is achieved when the relative delay between the received signal and the local replica of the PN sequence is zero. For any other delay (measured in increments of chips), the circular autocorrelation is  $-1$ , a factor of  $M$  smaller in magnitude than the peak of the correlation function. In order to match to the projected dimensions of a kilometer-sized pixel near the location of Tycho, range resolution of 750 m was selected by using a maximal-length binary PN sequence of 5  $\mu$ s chip duration, consisting of 2047 chips, modulated directly onto the carrier in a binary phase-shift keyed (BPSK) format. The return signal contained contributions from every illuminated range increment simultaneously. Signal components with different delays were separated out by correlating with a local replica of the transmitted PN sequence; an example of the correlation signature of the Tycho region is

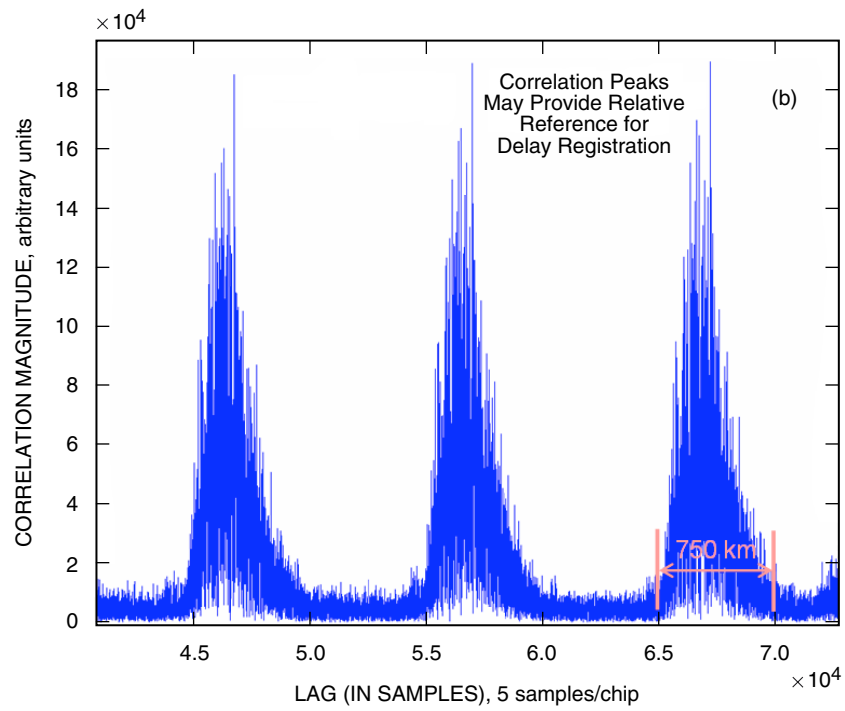
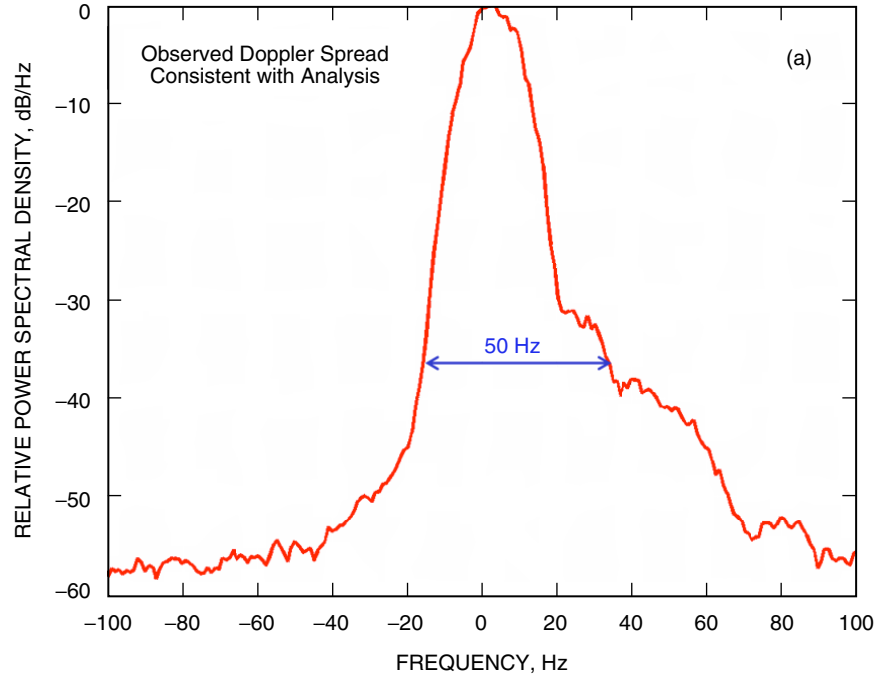


**Fig. 5. Signals received from the Tycho region: (a) Doppler-broadened unmodulated carrier received at Goldstone and (b) correlation signature of PN-modulated X-band signals.**

shown in Fig. 5(b) as a function of delay samples, corresponding to five samples per chip. Note that the same PN sequence is repeated continuously during transmission, resulting in a periodic correlation signature at the receiver.

The signal corresponding to each delay ring is further processed using an FFT to separate out pixels with different Doppler frequencies induced by lunar libration, in effect producing an estimate of the spectral content of each delay ring. When the intensity of the complex pixel values so obtained is plotted as a function of range and delay increments, a Doppler-delay image of the illuminated region is obtained. An example of the radar image with single-antenna illumination is shown in Fig. 6, clearly showing the crater Tycho near coordinates (0.0 Hz, 95 chips). Because of Doppler compensation, the frequency of the signal received from the target is at 7.15 GHz. When downconverted to complex baseband, the target always appears at 0.0 Hz in the FFT output. This image is an average of four processed 10-s data sequences, where a freely available alignment and stacking software (RegiStax) was used. Given one or more alignment points, software like RegiStax use correlation techniques to identify the alignment points across all of the images in the series. Once the locations of these points are identified, the software translates the individual images so that the desired features are aligned. In the case of Fig. 6, only one alignment point was selected (center of Tycho).

The Doppler-delay radar image shown in Fig. 6 can be transformed into a visually corrected version, as shown in Fig. 7(b). A corrected high-resolution image of the crater Tycho and its environs, published in [1], is shown for comparison in Fig. 7(a), approximately on the same scale. Although the angle of the radar illumination in these two cases was different, the crater Tycho, its central peak, and several nearby craters can be clearly identified in both images.

The corrected image was obtained by first applying a rotation (of approximately 45 deg), followed by a reduction in scale along one dimension. This first-order image correction was primarily for determining the most significant components of the transformation from Doppler-delay space to a Mercator projection.

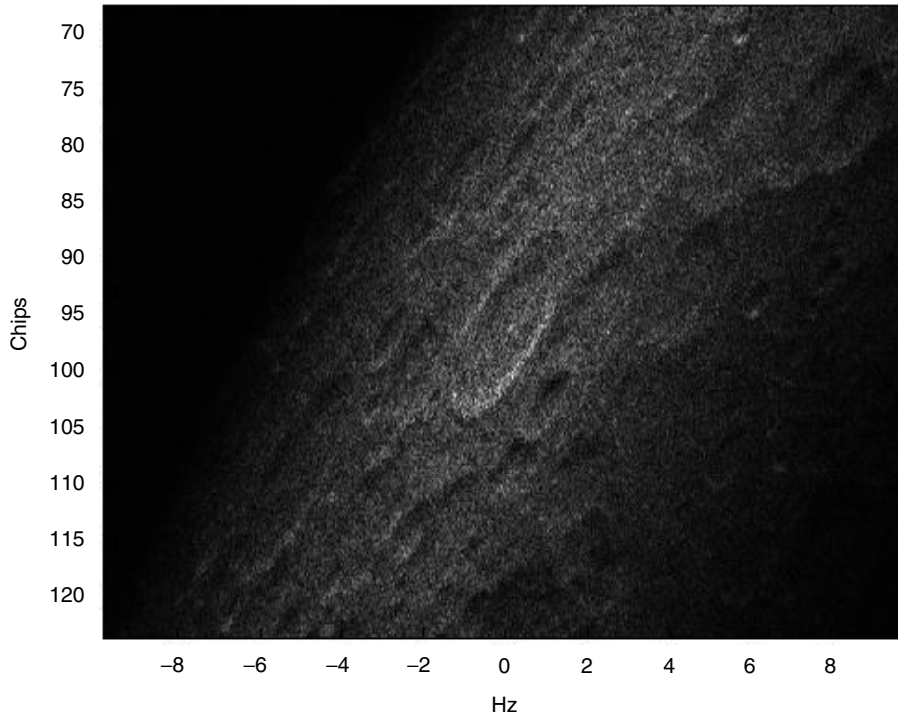


**Fig. 6. Single-antenna radar image of the Tycho region in Doppler-delay space.**

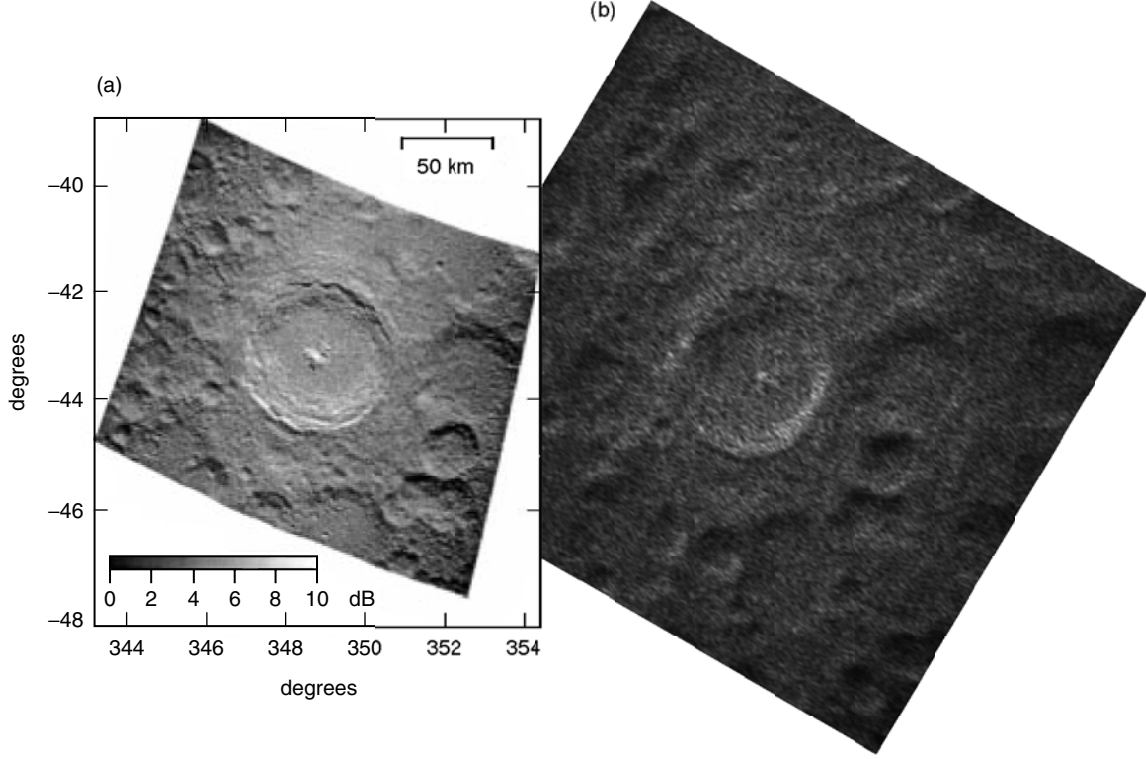


**Fig. 7. Tycho: (a) a high-resolution Doppler-delay radar image of the crater Tycho, taken from [1] with permission, corrected for range and Doppler distortions and (b) a first-order corrected version of Doppler-delay radar image of Fig. 6, showing similarity to rectified Mercator projection in (a).**

However, it should be emphasized that the original Doppler-delay image showing the target feature, as in Fig. 6, together with ephemerides for the target are perfectly adequate for the purposes of uplink array calibration.

When two antennas illuminate this region coherently at the same carrier frequency, a far-field array pattern consisting of bright and dark interference bands is formed. An example of the two-antenna array pattern and the resulting radar image can be seen in Fig. 8(a), with DSS 24 and DSS 25 transmitting. Distinctly different two-antenna patterns formed by the other two baselines are shown in Figs. 8(b) and 8(c).

Note that the experimentally obtained far-field patterns are projected onto the lunar sphere, instead of a normal plane at the distance of the Moon, as was the case in the simulations of Fig. 4. In addition, the experimental plots are in Doppler-delay space. Hence, they do not correspond exactly to the simulation results; however, the key features of the baseline patterns and the three-antenna pattern are clearly illustrated. For uplink array calibration, only the Doppler-delay images are needed; therefore, the additional transformation to Cartesian coordinates is not required.

When the Moon was simultaneously illuminated with all three antennas, the characteristic cross-hatched far-field pattern predicted by the simulation of Fig. 4 is evident, as shown in Fig. 9. Note the easily discernible walls and depression of the crater Tycho at coordinates (0 Hz, 350 chips) with the central peak close to a minimum of the three-antenna far-field pattern. Figures 8 and 9 are low-resolution images obtained in near real time by processing 10 s of data and were generated in approximately 1 minute in the field using a laptop computer in order to provide a quick-look capability for rough calibration.

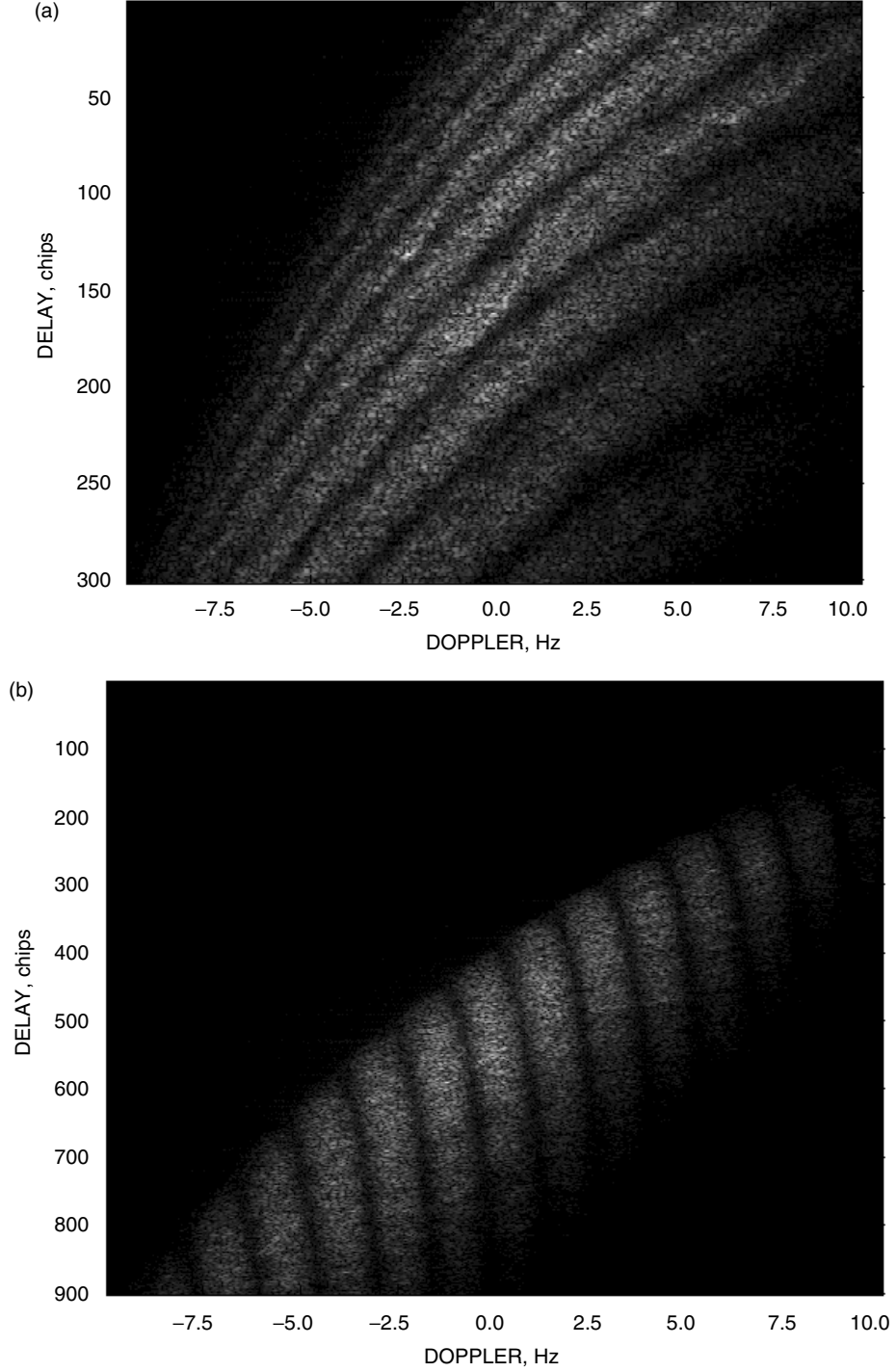


**Fig. 8. Tycho region illuminated by two antennas: (a) DSS 24 and DSS 25, (b) DSS 25 and DSS 26, and (c) DSS 24 and DSS 26. (a) shows characteristic interference bands in the far field. Tycho is near the center at coordinates (0 Hz, 150 chips). Each interference band cuts across both Doppler slices and range circles with this baseline geometry. (b) shows a different interference pattern in the far field due to the change in baseline geometry. Note that interference bands are essentially lined up with the Doppler slices, hence the apparent spin axis, of the Moon. (c) shows unique interference bands due to lunar curvature, cutting across two different Doppler slices at the same range (delay).**

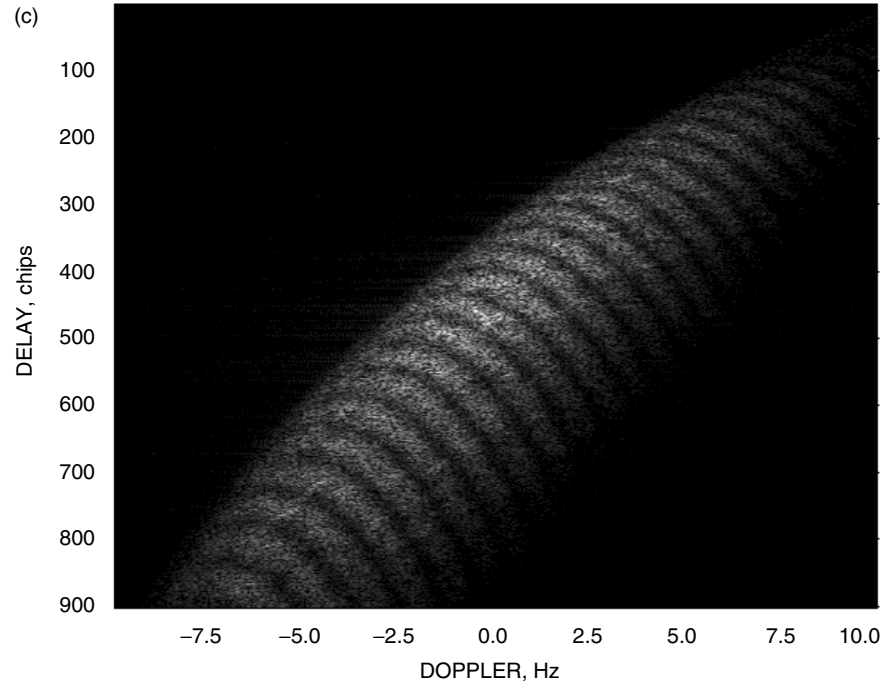


**Fig. 8 (contd).**

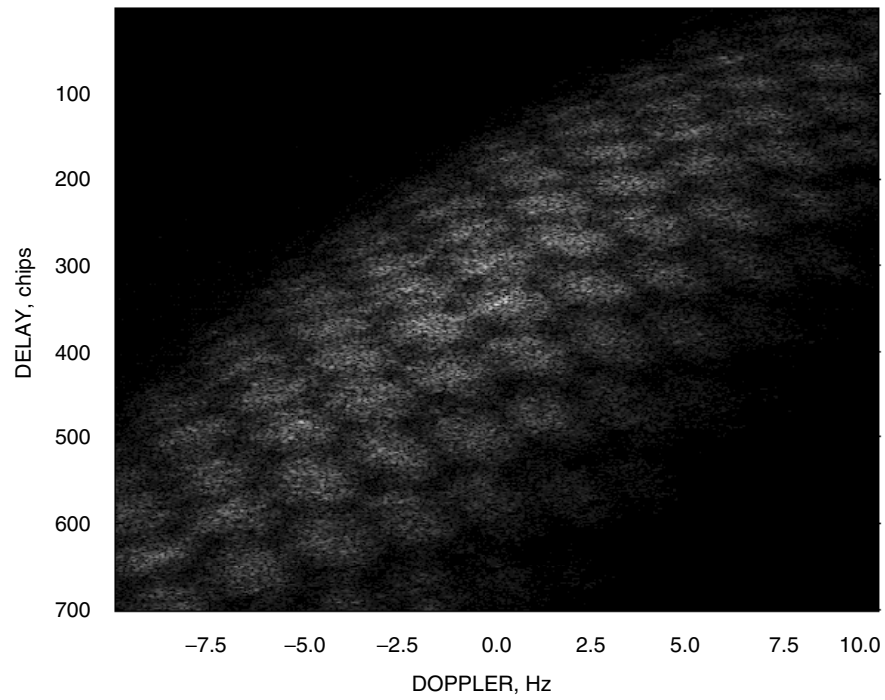


**Fig. 9. Three-antenna far-field pattern with easily discernible array lobes, corresponding well to the far-field pattern predicted by simulation.**



The experimentally obtained Doppler-delay radar images can be further improved by averaging several high-resolution images with independent scintillation profiles, resulting in the smoother picture shown in Fig. 10. This 30-s data sequence was processed with higher frequency resolution, requiring approximately 4 minutes of processing with the same laptop computer for each image. Images produced from the illumination of multiple antenna arrays are more difficult to align and stack because the high contrast of the far-field pattern often dominates lunar surface features. One work-around is to attempt a manual alignment, but this is difficult to do with pixel accuracy. Another, more successful technique is to locally amplify or reduce the contrast of the image before alignment and stacking. This adaptive contrast-enhancement technique improves the visibility of surface features and enables the alignment software to produce improved results.

The phase scale superimposed over the averaged image of Fig. 10 indicates a possible approach to calibrating two antennas. Since the nulls in the pattern are separated by  $2\pi$  rad of electrical phase, a simple linear scale spanning  $2\pi$  rad in the vicinity of the target can be used to estimate the phase difference between the antennas, in effect providing an estimate of the phase offset required to maximize the received power over the target pixel. It can be seen from Fig. 10 that the central peak of Tycho is close to zero phase difference in this image, indicating that an essentially phased-up condition existed when these data were recorded. Since the extent of the target is small compared to the array beamwidth (the distance between nulls in the two-antenna far-field pattern), and the ephemerides of this target are known to fractional arcsecond accuracy, two- or three-element arrays can be calibrated in this manner to an accuracy sufficient to demonstrate the calibration concept. Similar techniques can be applied to

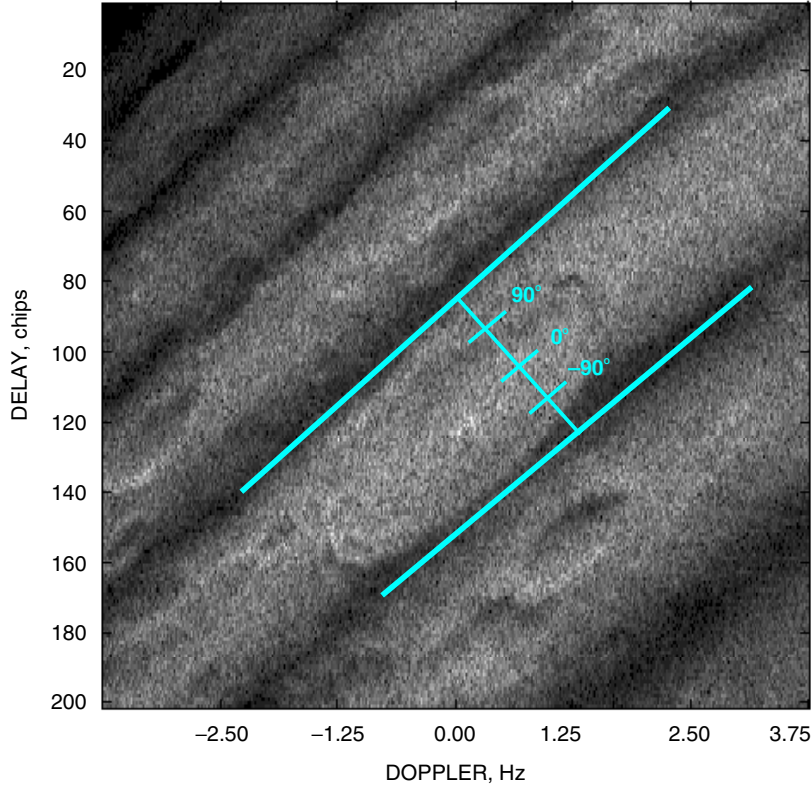


**Fig. 10.** Average of three high-resolution radar images of the crater Tycho, illuminated with a two-antenna array. The superimposed scale suggests a potential calibration technique for two antennas, as discussed in the text.



three-antenna arrays to obtain global maximization of the array power illuminating the target; hence, this calibration concept can be extended directly to arrays of three antennas. Arrays with a larger number of elements also could be calibrated by means of sequential application of the two-element technique, by first calibrating pairs of antennas, then treating each calibrated pair as a single entity, and repeating the process. The application of other power-maximization algorithms, including gradient descent and phase-retrieval techniques [5–7] to calibrate antenna arrays more efficiently, is the subject of current research.

## VI. Conclusions

The theoretical foundations of Doppler-delay radar imaging with arrays of antennas were developed in this article, and experimental results obtained with arrays of two and three 34-m antennas located at the Apollo Station were presented. The fundamental parameters pertinent to uplink array calibration by means of transmit-mode power maximization have been described and evaluated for a typical Moon-bounce example, and far-field array patterns were simulated using the actual antenna geometries in support of the experiments. The experiments consisted of transmitting Doppler-compensated, PN-sequence modulated 7.15-GHz carriers towards the crater Tycho on the Moon, whose central peak has a particularly high radio frequency reflection coefficient and whose ephemerides are known to the required accuracy for uplink array calibration applications. The experiments yielded stable and well-defined far-field patterns over the target with both two- and three-antenna arrays, validating the proposed Moon-bounce calibration concept. The results of these experiments demonstrate that uplink array calibration by means of far-field power maximization, using features on the Moon with well-known ephemerides as radar targets, is a viable calibration option for future operational uplink arrays.

## References

- [1] J.-L. Margot, D. Campbell, R. Jurgens, and M. Slade, “Digital Elevation Models of the Moon from Earth-Based Radar Interferometry,” *IEEE Transactions on Geoscience and Remote Sensing*, vol. 38, no. 2, pp. 1122–1133, March 2000.
- [2] V. Vilnrotter, R. Mukai, and D. Lee, “Uplink Array Calibration via Far-Field Power Measurement,” *The Interplanetary Network Progress Report*, vol. 42-164, Jet Propulsion Laboratory, Pasadena, California, pp. 1–16, February 15, 2006. [http://ipnpr/progress\\_report/42-164/164D.pdf](http://ipnpr/progress_report/42-164/164D.pdf)
- [3] J. V. Evans, “Radio Communication via the Moon,” *100 Years of Radio Conference Publication*, IEE, pp. 207–212, 1995.
- [4] T. Hargfors, “Remote Probing of the Moon by Infrared and Microwave Emissions and by Radar,” *Radio Science*, vol. 5, no. 2, pp. 189–227, 1970.
- [5] R. Mukai, K. Wilson, and V. Vilnrotter, “Application of Genetic and Gradient Descent Algorithms to Wavefront Compensation for Deep-Space Optical Communications Receiver,” *The Interplanetary Network Progress Report*, vol. 42-161, Jet Propulsion Laboratory, Pasadena, California, pp. 1–21, May 15, 2005. [http://ipnpr/progress\\_report/42-161/161U.pdf](http://ipnpr/progress_report/42-161/161U.pdf)
- [6] J. R. Fienup, “Phase Retrieval Algorithms: A Comparison,” *Applied Optics*, vol. 21, no. 15, pp. 2758–2769, August 1982.
- [7] R. Mukai, V. Vilnrotter, and C.-W. Lau, “Adaptive Wavefront-Correction Algorithms Using Focal-Plane Intensity Measurements,” *The Interplanetary Network Progress Report*, vol. 42-166, Jet Propulsion Laboratory, Pasadena, California, pp. 1–14, August 15, 2006. [http://ipnpr/progress\\_report/42-166/166D.pdf](http://ipnpr/progress_report/42-166/166D.pdf)